A model for the emergence of thermal plumes in Rayleigh-Bénard convection at infinite Prandtl number

By C. LEMERY[1], Y. RICARD[1] AND J. SOMMERIA[2]

[1]Laboratoire de Sciences de la Terre, ENSL, 46 , allée d'Italie, 69364 Lyon Cedex 07, France

[2] Laboratoire de Physique, ENSL, 46, allée d'Italie, 69364 Lyon Cedex 07, France

(Received 24 April 2000)

We propose a two-dimensional model of the three-dimensional Rayleigh-Bénard convection in the limit of very high Prandtl number and Rayleigh number, like in the earth mantle. The model equation describes the evolution of the first moment of the temperature anomaly in the thermal boundary layer, which is assumed thin with respect to the scale of motion. This two-dimensional field is transported by the velocity that it induces and is amplified by surface divergence. This model explains the emergence of thermal plumes, which arise as finite time singularities. We determine critical exponents for these singularities. Using a smoothing method we go beyond the singularity and reach a stage of developed convection. We describe a process of plume merging, leaving room for the birth of new instabilities. The heat flow at the surface predicted by our 2D model is found in good agreement with available data.

1. Introduction

Thermal plumes are ubiquitous in convection at high Rayleigh number, far from the threshold of instability (e.g. Nataf, 1991; Siggia, 1994). The development of a convective-plume from a localized source is a well-known process, and self-similar solutions of the equations of motion are available (Batchelor, 1954; Sparrow, Husar & Goldstein, 1970; Moses, Zocchi & Libchaber, 1993; Olson & Singer, 1993). However the *emergence* of a plume from a uniformly heated surface is not clearly understood. Plumes are strongly non-linear structures, out of reach of perturbative methods on the instability modes. Modeling the statistics of plume production and interactions is a challenge, and it is a central issue for predicting the heat flux average and its variability.

The aim of the present paper is to propose a model for the emergence of convective plumes and their further interactions. Our main hypothesis is that the fluid interior is well mixed, and temperature anomalies are restricted to a thermal boundary layer, which is thin in comparison with horizontal scales. This condition can be always satisfied for an appropriate initial condition: starting from a fluid at uniform temperature, we suddenly impose a different surface temperature θ_S (with a perturbation at large scale to initiate the instability). Then temperature diffuses within a thin boundary layer until convection is initiated, and thermal plumes emerge as singularities arising after a finite time in our boundary layer approximation.

Then the approximation breaks down: plumes are fully developed and feed the interior with temperature anomalies. However, we shall still capture the main features of

the dynamics with an appropriate phenomenological smoothing of the singularities. The further plume interactions will be described and the mean heat flux will be obtained by a numerical model with reduced dimensionality: a two-dimensional model on the horizontal heated surface represents the three-dimensional convection.

The development of a thermal plume is driven by the non-linearity in the heat transport equation, rather than by hydrodynamic turbulence, so this phenomenon can be conveniently analyzed in the limit of high Prandtl number, for which inertia is neglected. We therefore restrict our study to this limit of high Prandtl number, and we furthermore assume a free surface condition.

This convection regime ($Ra >> 1$, $Re << 1$ and $Pr >> 1$) corresponds to that of the silicated parts of Earth-like planetary interiors (e.g. Bercovici, Ricard & Richards 1998); as an example, for the Earth's mantle, i.e, the outer 3000 km of our planet, one has $Ra = 10^8$, $Re = 10^{-15}$ and $Pr = 10^{23}$.

In such planetary interiors, the viscosity increases by many orders of magnitude in the relatively thin upper layers, due to the lower temperature. Describing this rapid variation of viscosity with depth is a severe difficulty for full three-dimensional convective models. In our boundary layer model instead, this effect shows up as a viscosity of the 'surface skin'. Various rheologies of this surface skin could be implemented as well, accounting for the formation of rigid plates with complex fracturation properties, which are still out of reach of current convection models.

The general idea of this paper is to reduce the dimensionality of a convective system by integration of the dynamic equations across the boundary layers. Such a procedure has been fruitfully used to investigate the dynamics of bubbles (e.g. Pozrikidis, 1992) or the situations more akin to thermal convection as the Rayleigh-Taylor instability (Canright & Morris, 1993) and the Marangoni convection (Thess, Spirn & Jüttner, 1997). It is also a classical method in the geophysical literature to study the equilibrium of tectonic plates (Vilotte & Daignières, 1982; England & McKenzie, 1982; Houseman & England, 1986; Bird, 1988). However, the application to Rayleigh-Bénard convection where both the mechanical and thermal equations are integrated has never been done before and allows us to describe mathematically the destabilisation of the thermal boundary layers qualitatively explained by Howard (1966).

In next section, we present our boundary layer model. We first derive general relationships valid for any rheology, and then specify the model for a Newtonian fluid. We find that the effect of buoyancy in the thermal boundary layer results in a horizontal stress acting on the interior flow. This stress has formal similarities with surface tension effects in Marangoni convection, as analyzed by Thess *et al.* (1997). In their model, the surface temperature field induces a surface velocity field, obtained by solving the Stokes problem in the interior, with the boundary condition given by the viscous stress at the surface. Therefore the surface temperature is transported by a velocity which depends linearly, but non-locally, on the temperature field. The 'closure relationship' relating the surface velocity to temperature has a simple expression in Fourier space (but is non-local in real space). We find the same closure relationship as in the Marangoni case, but the active quantity is the first moment of the temperature in the boundary layer, instead of the surface temperature. This quantity is transported like temperature, but with an additional production term, which leads to the onset of singularities with infinite values, representing the thermal plumes. In Marangoni convection instead, the temperature remains finite, but its spatial derivatives become singular.

In section 3, we study the initial growth of our boundary layer by a linear stability analysis. In section 4 we discuss in detail the closure relationship giving the velocity field induced by different temperature fields. The properties of the singularities generated in

the model is discussed in section 5. Finally in section 6, we propose a simple phenomenological smoothing of the singularities, allowing to reach a permanent convective regime. Plumes (smoothed singularities) are observed to merge under the effect of their induced velocity field, and new plumes are formed between existing ones. We extend the model to two dimensions, representing 3D convection, with the formation of convective lines. The averaged heat flux is also calculated, and found in good agreement with numerical results found in the literature.

2. A 2D model of 3D Rayleigh-Bénard convection

2.1. *The 3D model*

We study thermal convection driven by buoyancy forces in the Boussinesq approximation. We assume that the Prandtl number, i.e., the ratio between the kinematic viscosity ν and thermal diffusivity κ is very large so that the Reynolds number is very small. In these conditions, the equations controlling the dynamic read:

$$\boldsymbol{\nabla} \cdot \boldsymbol{v} = 0, \tag{2.1}$$

$$\boldsymbol{\nabla} \cdot \boldsymbol{\tau} + \rho \boldsymbol{g} = 0, \tag{2.2}$$

$$\frac{\partial \theta}{\partial t} + (\boldsymbol{v} \cdot \boldsymbol{\nabla})\theta = \boldsymbol{\nabla} \cdot (\kappa \boldsymbol{\nabla} \theta). \tag{2.3}$$

They express respectively the conservation of mass, the balance of forces (neglecting inertia), and the heat transport. $\boldsymbol{\tau}$ denotes the total stress tensor, which will be related to the velocity $\boldsymbol{v}$ by an appropriate rheology, and $\boldsymbol{g}$ the acceleration of gravity. Equations (2.2) and (2.3) are coupled as the density ρ varies with temperature θ as $\rho = \rho_0(1 - \alpha\theta)$, with $\alpha\theta \ll 1$.

We consider for simplicity a uniform gravity (although our method readily extends to a spherical geometry). The surface is supposed infinite in the horizontal directions x and y. The z axis is directed downward and the convective system extends infinitely in the direction of positive z. The motion is driven by temperature anomalies near the surface, while the deep interior is supposed at uniform temperature. We choose this temperature as the reference temperature, so that $\theta \to 0$ for $z \to +\infty$ and θ reaches θ_S, which is negative, at the surface. Furthermore, since the motion is damped in the deep interior ($z \to +\infty$), the stress tensor reduces asymptotically to a pressure p_0, $\tau_{ij} \to -p_0 \delta_{ij}$, and equation (2.2) reduces to the hydrostatic relation $\boldsymbol{\nabla} p_0 = \rho_0 \boldsymbol{g}$, or $p_0 = \rho_0 g z$. The origin of the coordinate z is chosen in order to cancel the constant of integration which should appear in this expression. In other words, the free surface is at $z = 0$ in the reference state with $\theta = 0$ everywhere. We express the stress tensor $\boldsymbol{\tau}$ as the sum of the reference hydrostatic pressure and a stress τ', which is driven by the temperature heterogeneity θ and vanishes at large depth,

$$\tau_{ij} = \tau'_{ij} - \rho_0 g z \delta_{ij} \tag{2.4}$$

In summary, the conditions in the deep interior are

$$\boldsymbol{v} \to 0, \quad \tau'_{ij} \to 0, \quad \theta \to 0, \quad \text{for } z \to +\infty \tag{2.5}$$

For motion with sufficiently large horizontal scales, the stress $\boldsymbol{\tau}'$ reduces to the hydrostatic pressure associated with the temperature heterogeneity θ. Its typical value is

$\rho_0 g\alpha\theta H$, where H is the thickness of the thermal boundary layer, much smaller than the horizontal scale of motion L. The hydrostatic balance provides in all cases a first order estimate of the stress $\boldsymbol{\tau}'$,

$$|\boldsymbol{\tau}'| = o(\rho_0 g\alpha\theta H) \ll \rho_0 g H. \tag{2.6}$$

Due to the temperature heterogeneity θ, the free surface is slightly deformed, to a 'depth' $z = -h(x, y)$, much smaller than H, and the normal $\boldsymbol{n}$ to the surface is nearly vertical. The free surface condition imposes that the normal components of the total stress tensor vanish, $\boldsymbol{\tau}' \cdot \boldsymbol{n} + \rho_0 g h \boldsymbol{n} = 0$. With the estimates (2.6) for $|\tau'|$, it results that $h/H \sim \alpha\theta$. We can therefore take the stress tensor $\boldsymbol{\tau}'$ at $z = 0$ for the free surface condition, within an error of order $(\alpha\theta)^2$ (as estimated by linearizing $\boldsymbol{\tau}'$ with respect to z). Furthermore, the slope n_x/n_z (or n_y/n_z) is of order $h/L = \alpha\theta H/L$, and it can be safely neglected, so we can write the free surface conditions as

$$\tau'_{xz}(x, y, 0) = \tau'_{yz}(x, y, 0) = 0, \tag{2.7}$$

$$\tau'_{zz}(x, y, 0) = -\rho_0 g h(x, y). \tag{2.8}$$

It provides a free slip condition at $z = 0$ for the tangential stresses, while the normal component τ'_{zz} determines the weak topography $h(x, y)$. In addition to these dynamical conditions, we have the kinematic condition for a material surface, which reduces to

$$v_z(x, y, 0) = 0 \tag{2.9}$$

within our approximations.

In summary, the three components of the equation of motion (2.2) write,

$$\partial_x \tau'_{xx} + \partial_y \tau'_{xy} + \partial_z \tau'_{xz} = 0, \tag{2.10}$$

$$\partial_x \tau'_{yx} + \partial_y \tau'_{yy} + \partial_z \tau'_{yz} = 0, \tag{2.11}$$

$$\partial_x \tau'_{zx} + \partial_y \tau'_{zy} + \partial_z \tau'_{zz} = \rho_0 \alpha g \theta. \tag{2.12}$$

They must be solved together with (2.1) and (2.3), using the appropriate rheology, and with the boundary conditions (2.5),(2.7),(2.8) and (2.9).

2.2. *Integration of the stress across the boundary layer*

The thermal boundary layer entrains the interior like a 'skin' driven by gravity effects, and this process can be described by integrating the equations of motion across the boundary layer. We denote $\bar{X}$ the z-integrated value of a quantity X, from $z = 0$ to the depth Z. We first get exact equations, but will then assume that Z is much smaller than the horizontal scale of motion L, while beyond the boundary layer (where $\theta \approx 0$), $H \lesssim Z \ll L$.

Such a vertical integration, applied to the vertical component of the equation of motion (2.12), yields, using the free surface condition (2.8),

$$\partial_x \bar{\tau}'_{zx} + \partial_y \bar{\tau}'_{zy} + \tau'_{zz} + \rho_0 g h = \rho_0 g \alpha \overline{\theta}, \tag{2.13}$$

giving the topography $-h(x, y)$ from the dynamical variables. Applying this relation to the deep interior, $z \to +\infty$, τ'_{zz} vanishes. For sufficiently large scales, the horizontal derivatives become negligible, and (2.13) reduces to $h = \alpha\bar{\theta}$, which simply expresses Archimedes principle, also called isostasy among geophysicists.

To get a constraint on the dynamical variables, we multiply all terms of (2.12) by z before the vertical integration, yielding

$$\partial_x \overline{z\tau'_{zx}} + \partial_y \overline{z\tau'_{zy}} + Z\tau'_{zz} - \bar{\tau}'_{zz} = \rho_0 g\alpha \overline{z\theta}, \tag{2.14}$$

(where we have used an integration by part for the term in τ'_{zz}). The last term of the left hand side dominates the three first terms. Therefore, relation (2.14) relates the average vertical stress in the boundary layer to the first moment of the temperature. This behavior has already been emphasized in the geophysical literature and equation (2.14) has been sometimes called 'stress moment law' (Fleitout & Froidevaux 1982,1983; Ricard, Fleitout & Froidevaux 1984).

We similarly integrate the horizontal components (2.10) and (2.11) of the momentum equation, using the free surface condition (2.7),

$$\partial_x \overline{\tau'_{xx} - \tau'_{zz}} + \partial_y \overline{\tau'_{xy}} + \tau'_{xz} = -\partial_x \overline{\tau'_{zz}}, \tag{2.15}$$

$$\partial_x \overline{\tau'_{xy}} + \partial_y \overline{\tau'_{yy} - \tau'_{zz}} + \tau'_{yz} = -\partial_y \overline{\tau'_{zz}}. \tag{2.16}$$

We have written the two equations so that their left-hand side depend only on the deviatoric part of the stress tensor, which will be related to the velocity once the rheology is specified (in other words the pressure term has been eliminated on the left-hand side).

The right hand side of (2.15) and (2.16) can be related by (2.14) to the temperature moment, which we define as

$$M \equiv -\overline{z\theta} \tag{2.17}$$

$$\equiv -\int_0^\infty z\theta \, dz, \tag{2.18}$$

the sign minus is introduced to get M positive in the convection problem. Then (2.15) becomes

$$\tau'_{xz} + Z\partial_x \tau'_{zz} + \partial_x \overline{\tau'_{xx} - \tau'_{zz}} + \partial_y \overline{\tau'_{xy}} + \partial_x \partial_x \overline{z\tau'_{zx}} + \partial_x \partial_y \overline{z\tau'_{zy}} = -\rho_0 g\alpha \partial_x M. \tag{2.19}$$

All terms in the left-hand side depend only on the deviatoric part of the stress tensor, except the second term $Z\partial_x \tau'_{zz}$. We can rearrange this term by writing $\partial_x \tau'_{zz} = \partial_x(\tau'_{zz} - \tau'_{xx}) + \partial_x \tau'_{xx}$, and, using (2.10), $\partial_x \tau'_{xx} = -\partial_y \tau'_{xy} - \partial_z \tau'_{xz}$. Introducing this in (2.19), and repeating the same procedure for the y component, (2.15) and (2.16) transform into

$$\tau'_{xz} - Z\partial_z \tau'_{xz} + \partial_x[\overline{\tau'_{xx} - \tau'_{zz}} - Z(\tau'_{xx} - \tau'_{zz})] + \partial_y[\overline{\tau'_{xy}} - Z\tau'_{xy}] + \\ + \partial_x \partial_x \overline{z\tau'_{zx}} + \partial_x \partial_y \overline{z\tau'_{zy}} = -\rho_0 g\alpha \partial_x M, \tag{2.20}$$

$$\tau'_{yz} - Z\partial_z \tau'_{yz} + \partial_y[\overline{\tau'_{yy} - \tau'_{zz}} - Z(\tau'_{yy} - \tau'_{zz})] + \partial_x[\overline{\tau'_{xy}} - Z\tau'_{xy}] + \\ + \partial_y \partial_y \overline{z\tau'_{zy}} + \partial_x \partial_y \overline{z\tau'_{zx}} = -\rho_0 g\alpha \partial_y M, \tag{2.21}$$

which provides exact relations between the deviatoric part of the stress tensor, integrated over the ordinate range $[0, Z]$, and the first temperature moment M.

The left-hand side of these equations is clearly dominated by the first term, the other terms bringing corrections with relative magnitude Z/L and $(Z/L)^2$ (remembering that $\overline{X} \sim ZX$). Thus (2.20) and (2.21) state at first order that the thermal boundary layer drives the interior flow with a horizontal surface stress (τ'_{xz}, τ'_{yz}) proportional to the gradient of M on the surface. This is analogous to the free surface condition in Marangoni convection, for which M should be replaced by the surface temperature. Furthermore, we shall see in subsection 2.4 that M is advected by the horizontal flow, like a temperature

(however there is an additional production term for M, proportional to the horizontal flow divergence, so the analogy with Marangoni convection is not exact).

Before proceeding further, it is useful to consider corrections of order Z/L on the left-hand side of (2.20) and (2.21). The second term $-Z\partial_z\tau'_{xz}$ can be viewed as a correction to linearly extrapolate τ'_{xz} from its value at depth $z = Z$ to $z = 0$. Therefore the boundary layer really acts as a surface skin at position $z = 0$, instead of the arbitrary position Z. The next two terms are related to horizontal shear effects, describing an horizontal viscosity of the surface skin. Finally, the last two terms are clearly of order $(Z/L)^2$ with respect to τ'_{xz} or τ'_{yz}, and can be neglected.

To get explicit results, we now assume a Newtonian rheology, with a viscosity η,

$$\tau'_{ij} = \eta(\partial_i v_j + \partial_j v_i) - p\delta_{ij}. \tag{2.22}$$

This viscosity is possibly non-uniform in the boundary layer, beyond which it reaches a uniform value η_0. We introduce the relative excess 'surface' viscosity

$$\sigma = \int_0^Z \frac{\eta(z) - \eta_0}{\eta_0} dz, \tag{2.23}$$

which becomes independent of the upper bound Z when it is beyond the boundary layer (since the integrand tends to 0). Introduction of this rheology in (2.20) and (2.21), expressing $\partial_z v_z = -\partial_x v_x - \partial_y v_y$ from the incompressibility condition, and considering that v_x and v_y can not depend on z over the boundary layer at first order, we get

$$-\partial_z v_x - 2\partial_x[\sigma(2\partial_x v_x + \partial_y v_y)] - \partial_y[\sigma(\partial_x v_y + \partial_y v_x)] = \frac{\rho_0 g\alpha}{\eta_0}\partial_x M, \tag{2.24}$$

$$-\partial_z v_y - 2\partial_y[\sigma(2\partial_y v_y + \partial_x v_x)] - \partial_x[\sigma(\partial_x v_y + \partial_y v_x)] = \frac{\rho_0 g\alpha}{\eta_0}\partial_y M. \tag{2.25}$$

The first terms of these two equations, $\partial_z v_x$ and $\partial_z v_y$ provide the stresses transmitted to the interior, i.e. the z-derivatives of the horizontal velocities for the internal flow taken at $z = 0$. These stresses are non-zero even though v_x and v_y in the boundary layer do not depend on z at first order.

As in usual fluid dynamics, we can decompose the horizontal strain into a traceless strain tensor $\mathbf{T}$ and a horizontal divergence,

$$\mathbf{T}_{xx} = -\mathbf{T}_{yy} = \partial_x v_x - \partial_y v_y, \tag{2.26}$$

$$\mathbf{T}_{xy} = \mathbf{T}_{yx} = \partial_x v_y + \partial_y v_x. \tag{2.27}$$

Then, denoting the horizontal velocity vector by $\boldsymbol{v}_H$ and the horizontal nabla operator by $\boldsymbol{\nabla}_H$, equations (2.24) and (2.25) can be written as

$$-\partial_z \boldsymbol{v}_H - \boldsymbol{\nabla}_H \cdot (\sigma\mathbf{T}) - \boldsymbol{\nabla}_H(3\sigma\boldsymbol{\nabla}_H \cdot \boldsymbol{v}_H) = \frac{\rho_0 g\alpha}{\eta_0}\boldsymbol{\nabla}_H M. \tag{2.28}$$

It provides boundary conditions at $z \to 0$ for the interior flow. The effect of the boundary layer on the interior is therefore equivalent to a surface skin providing a stress proportional to the horizontal gradient of M, with a two-dimensional shear viscosity $\sigma\eta_0$ and a compressional viscosity $3\sigma\eta_0$.

2.3. *The interior flow*

In the interior, the temperature heterogeneity θ vanishes, and we assume a constant viscosity η_0, so that the momentum equation (2.2) reduces to the Stokes equation,

$$\eta_0\nabla^2\boldsymbol{v} - \boldsymbol{\nabla}p = 0. \tag{2.29}$$

This equation must be solved, together with the incompressibility equation (2.1), with the conditions of decaying motion at $z \to +\infty$, and the boundary conditions at $z = 0$ provided by (2.28).

This problem is classically solved (see Chandrasekhar 1981) in terms of the vertical velocity v_z and vertical vorticity $\Omega_z = \partial_x v_y - \partial_y v_x$. These two quantities determine the poloidal and toroidal parts of the velocity field respectively, i.e. the Helmholtz decomposition of the horizontal velocity projection $\boldsymbol{v}_H$ in each horizontal plane,

$$\boldsymbol{v}_H = \boldsymbol{\nabla}_H \phi - \boldsymbol{e}_z \times \boldsymbol{\nabla}_H \psi, \tag{2.30}$$

where the first term is irrotational and the second term is non-divergent ($\boldsymbol{e}_z$ is the vertical unit vector). The two scalars ϕ and ψ are obtained from v_z and Ω_z by solving the Poisson equations, obtained by taking the horizontal divergence and the curl of (2.30) respectively,

$$\nabla_H^2 \phi = -\partial_z v_z, \tag{2.31}$$

$$\nabla_H^2 \psi = -\Omega_z. \tag{2.32}$$

For a velocity field with a harmonic horizontal dependence, $\boldsymbol{v} = \hat{\boldsymbol{v}}(z) e^{\mathrm{i}\boldsymbol{k}\cdot\boldsymbol{r}}$ with $\boldsymbol{k} = (k_x, k_y)$, these relations yield (with $k \equiv |\boldsymbol{k}|$),

$$\hat{v}_x = \frac{\mathrm{i}}{k^2}\left(k_x \frac{d\hat{v}_z}{dz} + k_y \hat{\Omega}_z\right), \tag{2.33}$$

$$\hat{v}_y = \frac{i}{k^2}\left(k_y \frac{d\hat{v_z}}{dz} - k_x \hat{\Omega}_z\right). \tag{2.34}$$

Taking the curl of (2.29) eliminates the pressure and yields $\nabla^2 \Omega_z = 0$, or equivalently

$$(\partial_z^2 + \nabla_H^2)\Omega_z = 0. \tag{2.35}$$

Taking the divergence of (2.29) yields $\nabla^2 p = 0$ (taking into account the flow incompressibility). Then taking the Laplacian of (2.29) yields $\nabla^4 \boldsymbol{v} = 0$, whose z component writes

$$(\partial_z^2 + \nabla_H^2)^2 v_z = 0. \tag{2.36}$$

Solutions with a sine wave horizontal dependence of (2.35) and (2.36), which vanish for $z \to +\infty$, are respectively,

$$\hat{v}_z \;=\; u\; z\; \exp(-kz), \tag{2.37}$$

$$\hat{\Omega}_z = w \exp(-kz). \tag{2.38}$$

Then the horizontal velocity components $\hat{v}_x$ and $\hat{v}_y$ are obtained from (2.33) and (2.34).

The boundary condition (2.28) at $z = 0$ is easily taken into account in the case of a uniform surface viscosity σ. Taking the horizontal divergence and curl of (2.28) then yield respectively,

$$\eta_0(\partial_z + 4\sigma\nabla_H^2)\partial_z v_z = \rho_0 g \alpha \nabla_H^2 M, \tag{2.39}$$

$$(\partial_z + \sigma\nabla_H^2)\Omega_z = 0. \tag{2.40}$$

Therefore the toroidal mode is not excited by convection for σ uniform ($\Omega_z = 0$ everywhere). Introducing expression (2.37) into (2.39) yields $2\eta_0(1+2\sigma k)u = \mathrm{sign}(k)\rho_0 g \alpha k M$.

The resulting relationships relating the surface velocity to the Fourier transform $\hat{M}(\boldsymbol{k})$ of the temperature moment can be written

$$\hat{\boldsymbol{v}}_H(k) = \mathrm{i}\frac{\boldsymbol{k}}{2k}\frac{1}{1+2\sigma k}\frac{\rho_0 g\alpha}{\eta_0}\hat{M}(\boldsymbol{k}). \tag{2.41}$$

In this section we have assumed that below the thermal boundary layer the viscosity is uniform. However it would have been straightforward to develop a model with a vertically stratified viscosity at depth. For instance, if the interior is layered, equations (2.35) and (2.36) remain valid in each layer, but continuity of velocities and stresses must be imposed at each interface. Whatever the viscosity stratification, we would have obtained a linear relationship between the Fourier components of the surface velocity and those of the temperature moment with no excitation of toroidal motions. Thus, with minor modifications, our approach could be applied to planetary interiors where the viscosity is likely to increase with depth.

2.4. *The transport of the first temperature moment*

Since temperature acts only through its first moment M, it is useful to get an evolution equation for this quantity by taking the first moment of (2.3),

$$\frac{\partial M}{\partial t} + (\boldsymbol{v}_H \cdot \boldsymbol{\nabla}_H)M - \int_0^{+\infty} z v_z \frac{\partial \theta}{\partial z}\, dz = \boldsymbol{\nabla}_H(\kappa \boldsymbol{\nabla}_H M) - \int_0^{+\infty} z\frac{\partial}{\partial z}(\kappa\frac{\partial \theta}{\partial z})\, dz. \tag{2.42}$$

In this equation we have permuted $\boldsymbol{v}_H$ and the vertical integration, assuming that $\boldsymbol{v}_H$ does not depend on z in the boundary layer, which is valid at order (H/L). This assumption also implies, by integration of the mass conservation equation (2.1), that $v_z = -z\boldsymbol{\nabla}_H \cdot \boldsymbol{v}_H$. Thus, using integrations by part, and reminding that both θ and $\partial\theta/\partial z$ tend to zero for $z \to +\infty$, and that $\theta = \theta_S$ at $z = 0$, we transform (2.42) into,

$$\frac{\partial M}{\partial t} + (\boldsymbol{v}_H \cdot \boldsymbol{\nabla}_H)M + 2M\boldsymbol{\nabla}_H \cdot \boldsymbol{v}_H = \kappa\nabla_H^2 M - \kappa\theta_S, \tag{2.43}$$

(assuming κ constant). Therefore we have transformed a 3D problems with 4 unknowns, θ and the three components of $\boldsymbol{v}$, (equation (2.1)(2.2)(2.3)) into a 2D problem with 3 unknowns, M and the two components of $\boldsymbol{v}_H$. To close the system we need to relate $\boldsymbol{v}_H$ to M, using (2.41) that will now be referred to as the 'closure law'.

To elucidate the physical meaning of M, we assume that the temperature is simply described by $\theta = \theta_S$ erfc(z/H(x, y, t)), where erfc is the complementary error function, and H the thickness of the thermal boundary layer. Introduction of this temperature dependence in the definition of M (2.18) leads to

$$M(x, y, t) = -\frac{1}{4}\,\theta_S H^2(x, y, t), \tag{2.44}$$

which shows that $(M)^{\frac{1}{2}}$ is a measure of the thermal boundary thickness.

The first term of equation (2.43) is equal to $2(M)^{\frac{1}{2}}(\partial(M)^{\frac{1}{2}}/\partial t)$ and the second and third term can be combined together as $2(M)^{\frac{1}{2}}\boldsymbol{\nabla}_H((M)^{\frac{1}{2}}\boldsymbol{v}_H)$ so that equation (2.43) can be expressed as a transport equation for the quantity $(M)^{\frac{1}{2}}$.

By integration of this transport equation over the whole surface, we get

$$\frac{\mathrm{d}}{\mathrm{d}t}\iint (M)^{\frac{1}{2}}\, d^2\boldsymbol{r} = \frac{\kappa}{4}\iint \frac{(\boldsymbol{\nabla}_H M)^2}{(M)^{\frac{3}{2}}}\, d^2\boldsymbol{r} - \frac{\kappa}{2}\iint \frac{\theta_s}{(M)^{\frac{1}{2}}}\, d^2\boldsymbol{r}. \tag{2.45}$$

We remark that the left hand-side is conserved when κ is zero. This is not surprising as $(M)^{\frac{1}{2}}$ is proportional to the thickness of the boundary layer (2.44) and thus the previous

equation expresses the conservation of the boundary layer volume in the absence of diffusion. The thermal diffusion increases the volume of the boundary layer by cooling at the surface, especially when the boundary layer is thin (the term $-\theta_s/(M)^{\frac{1}{2}}$ is large); and by lateral diffusion acting on the boundary layer undulations.

In the case $\sigma = 0$, the closure law reduces to $\hat{\boldsymbol{v}}_H = \mathrm{i}(\boldsymbol{k}/2k)\hat{M}$. This is analogous to the result of Thess *et al.* (1997) for Marangoni convection, where M would be replaced by the surface temperature. However the equation (2.43) differs from a usual transport equation by the term $2M\boldsymbol{\nabla}_H \cdot \boldsymbol{v}_H$. When instability develops, this term will be a strong source of M, leading to a peak with diverging M, corresponding to the emergence of a thermal plume. Thess *et al.* (1997) also find the development of singularities in Marangoni convection, but the transported quantity (temperature) remains bounded.

3. Stability analysis

3.1. *Non-dimensionalisation*

It is convenient to get a non-dimensional version of our dynamical model, defining a length scale D by

$$D^3 = -\frac{\eta_0 \kappa}{\rho_0 g \alpha \theta_S}, \tag{3.1}$$

(θ_S is negative). This is the thickness for which the Rayleigh number, based on the vertical temperature difference θ_S, is unity. The time is then scaled by the diffusive time-scale (D^2/κ) and the temperature moment M by $-\theta_S D^2$. Using parameters applicable for the Earth D would be of order 10 km, the time scale about 3 Myrs and the moment scale about 1.5 10^5 K.km^2. With this change of variables we obtain

$$\frac{\partial M}{\partial t} + (\boldsymbol{v}_H \cdot \boldsymbol{\nabla}_H)M + 2M\boldsymbol{\nabla}_H \cdot \boldsymbol{v}_H = \boldsymbol{\nabla}^2 M + 1, \tag{3.2}$$

$$\text{with} \quad \hat{\boldsymbol{v}}_H(\boldsymbol{k}) = \mathrm{i}\frac{\boldsymbol{k}}{2k} \ \frac{\hat{M}(\boldsymbol{k})}{1 + 2\sigma k}, \tag{3.3}$$

where for simplicity of notation we have kept the same symbols for the new quantities which are now without units. In the case $\sigma = 0$, the equation becomes universal, i.e. without any parameter.

We have written a numerical code solving the two previous equations (3.2) and (3.3). This pseudo-spectral code uses a fast Fourier transform with at most $(512)^2$ points in 1D or 2D and assumes periodicity. This code has been parallelized on 16 processors. As an initial condition we assume that M, either one or two dimensional, consists in a small amplitude white noise with a positive small average value (M is everywhere positive). The moment M always follows the typical evolution depicted in Figure 1. The average value of M, $< M >$ increases linearly with time and its perturbations $\max |M - < M >|$ starts to decrease (diffusive regime) then increases slowly (marginal growth) and reaches a finite-time singularity. The duration of each period depends on the initial conditions and the values of σ.

3.2. *Marginal stability*

A first insight on the behavior of our boundary layer model of Rayleigh-Bénard convection will be given by a marginal stability analysis. Let us assume that $M(x,t) = M_0(t) + m(k,t)\cos(kx)$ with $|m| << |M_0|$ and $M_0(0) = 0$, so that we start with a viscous half-space at zero temperature on which we suddenly impose a surface negative temperature.

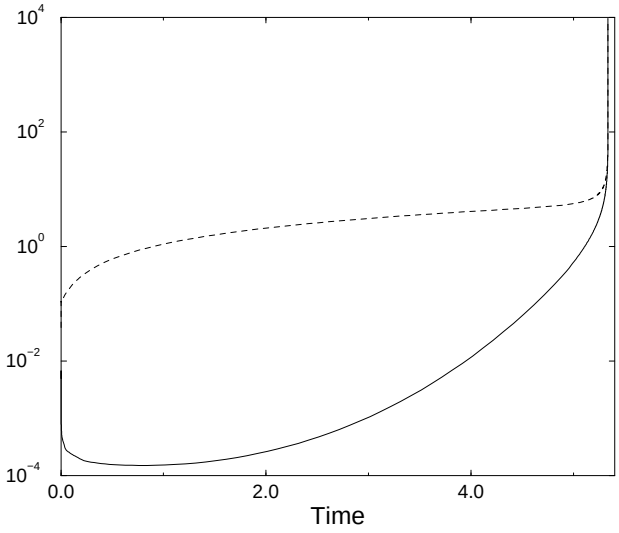

FIGURE 1. *Typical evolution of the averaged moment* $< M >$ *(dashed line) and the maximum of its fluctuation* $\max|M - < M >|$ *(solid line).* $< M >$ *increases linearly with time at the beginning (which is not obvious in this linear-logarithmic plot). Three phases are seen for the fluctuations: a decrease, a slow increase, and a finite-time instability. In this simulation we have assumed* $\sigma = 0$*, but qualitatively the same behavior is observed for non zero* σ*.*

For simplicity, we first assume that $\sigma = 0$. By plugging the expression of M into equations (3.2) and (3.3), linearized with respect to the small amplitude m, we get

$$M_0(t) = t, \tag{3.4}$$

$$\frac{\partial m}{\partial t} = k(t - k)m. \tag{3.5}$$

The growth-rate factor of (3.5) is depicted in Figure 2 at a given time. Equation (3.5) shows that all wave-numbers between $k = 0$ and $k = t$ are unstable. The most unstable is the wavenumber $k_m = t/2$. The destabilization of the system thus starts at long-wavelength. This justifies our long-wavelength approximation, at least in the initial stage of the evolution.

Recording that (in real units) $M_0 \sim -\frac{1}{4}\theta_S H^2$ (2.44) where H is the thickness of the thermal boundary layer, equation (3.4) simply says in real units that:

$$H^2 = 4\kappa t, \tag{3.6}$$

which just expresses the diffusive growth of the thermal boundary layer. The selection of the most unstable wavenumber can be rewritten

$$k_m H = -\frac{1}{4}\frac{\rho_0 \alpha g \theta_S H^3}{\eta_0 \kappa}, \tag{3.7}$$

stating that the most unstable wavenumber, normalized by the boundary layer thickness, is one fourth of the local Rayleigh number (which increases with $t^{\frac{3}{2}}$).

Equation (3.5) can be easily integrated, for a given k

$$m(t) = m_0 \exp[kt(\frac{t}{2} - k)] \tag{3.8}$$

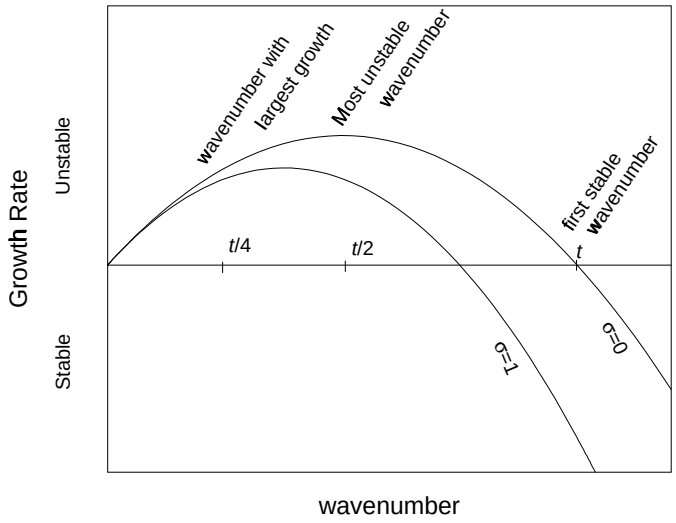

FIGURE 2. *Growth rate as a function of wavenumber (at a given time t) for a uniform viscosity fluid ($\sigma = 0$) or with a viscous lid ($\sigma = 1$).*

The amplitude at any wavenumber first decreases by thermal diffusion then increases when the boundary layer is sufficiently thick to sustain the instability. At a given time, the wavelength perturbation that has grown most strongly corresponds to $k = t/4$. Assuming that in the white-noise initial conditions all wavenumbers had equal amplitudes, the perturbation maximum is roughly controlled by the wave-number that has grown the most, therefore,

$$\max m(t) \sim m_0 \exp\left(\frac{t^3}{16}\right), \tag{3.9}$$

or in real units

$$\max m(t) \sim m_0 \exp\left(\frac{1}{128}\frac{H^6}{D^6}\right). \tag{3.10}$$

This linear analysis is valid as long as $|m(t)| << M_0(t)$, i.e. as long as in figure 1 the continuous line ($|m(t)|$) stays below the dashed line ($M_0(t)$).

We can verify numerically these analytic solutions. Figure 3 represents the same data set as Figure 1, $\max_x\ [M(x,t)]$ but this time as a function of t^3. The numerical solution shows an excellent fit to the analytical expression.

In the case $\sigma \neq 0$, when additional viscous effects are present in the boundary layer, this marginal stability analysis has to be somewhat modified. The instantaneous growth-rate is decreased together with the range of unstable wavevectors (see Figure 2). Equation (3.9) has to be corrected and one gets at first order

$$m(t) = m_0 \exp\left(\frac{t^3}{16}\frac{1}{1+\sigma t}\right), \tag{3.11}$$

this instability growth is therefore slowed down by the effect of a viscous lid and we see numerically that the time for the singularity to occur, increases. Although equation (3.11) is qualitatively in agreement with the numerical experiments, quantitatively the

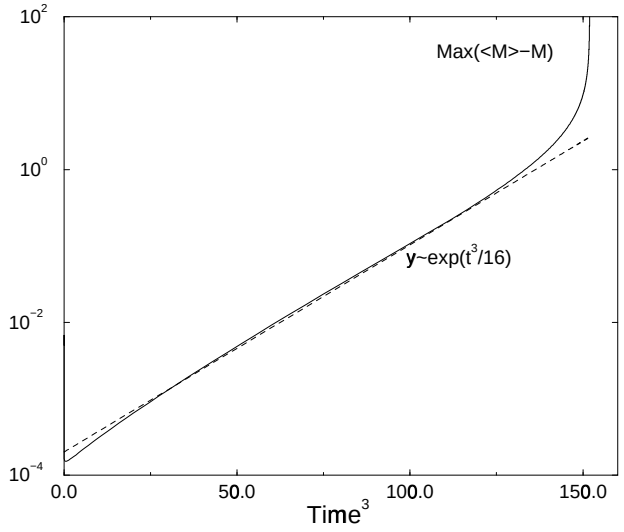

FIGURE 3. $\max|M - < M >|$ *as a function of* t^3. *Starting from a white noise, the slope is 1/16 according to equation (3.9).*

agreement is poor as σt is rapidly of order unity and a higher order expansion should be done.

4. The closure relationship

4.1. *Back in real space*

From Figures 1 or 3, it seems obvious that the system exhibits finite time singularities. In order to describe what happens closer to this singularity, we must study in the real space our closure relationship (3.3). The multiplication of Fourier components corresponds to a convolution product in real space assuming that the surface of the fluid is unbounded

$$\boldsymbol{v}_H(\boldsymbol{r}) = \iint \boldsymbol{K}(\boldsymbol{r}-\boldsymbol{r}')M(\boldsymbol{r}')d^2\boldsymbol{r}', \tag{4.1}$$

where $\boldsymbol{K}(\boldsymbol{r})$ is the Fourier transform of $i(\boldsymbol{k}/2k)\ (1+2\sigma k)^{-1}$. We will consider the two limiting cases, $\sigma = 0$, and $\sigma \gg 1$.

In the first case, one has $\hat{\boldsymbol{v}}_H = i(\boldsymbol{k}/2k)\hat{M}$, like described by Thess *et al.* (1997) for Marangoni convection. In real space the velocity is expressed as

$$\boldsymbol{v}_H(\boldsymbol{r}) = -\frac{1}{4\pi}\iint \frac{\boldsymbol{r}-\boldsymbol{r}'}{|\boldsymbol{r}-\boldsymbol{r}'|^3}M(\boldsymbol{r}')\ d^2\boldsymbol{r}' \equiv \mathcal{V}_0[M(\boldsymbol{r})], \tag{4.2}$$

defining the non-local operator $\mathcal{V}_0$ relating the velocity field to the M field. This integral (4.2) as well as various other integrals that will be used in the next paragraphs must be understood in terms of Cauchy principal value determination. The kernel $\boldsymbol{K}(\boldsymbol{r}) = -1/(4\pi)\boldsymbol{r}/|\boldsymbol{r}|^3 = 1/(4\pi)\boldsymbol{\nabla}(1/r)$ is formally identical to the Green function for the Laplacian with forcing at the boundary. The operator $\mathcal{V}_0$ is linear and is invariant by a change of scale $\boldsymbol{r} \to \beta\boldsymbol{r}$, reflecting the fact that convection of a half space (infinite layer) has no

internal length-scale,

$$\begin{aligned} \mathcal{V}_0[\alpha M] &= \alpha \mathcal{V}_0[M], \\ \mathcal{V}_0[M(\beta \boldsymbol{r})] &= \mathcal{V}_0[M(\boldsymbol{r})]. \end{aligned} \tag{4.3}$$

In the opposite case $\sigma \gg 1$, the closure relation writes in Fourier space, $\hat{\boldsymbol{v}}_H(\boldsymbol{k}) = (\mathrm{i}\boldsymbol{k}/4\sigma k^2)\hat{M}(\boldsymbol{k})$. By multiplying this equation by $\mathrm{i}\boldsymbol{k}$, we deduce that

$$\boldsymbol{\nabla}_H \cdot \boldsymbol{v}_H = -\frac{M}{4\sigma}, \tag{4.4}$$

which has the solution

$$\boldsymbol{v}_H(\boldsymbol{r}) = -\frac{1}{8\pi\sigma} \iint \frac{\boldsymbol{r}-\boldsymbol{r}'}{|\boldsymbol{r}-\boldsymbol{r}'|^2} M(\boldsymbol{r}')\, d^2\boldsymbol{r}' \;\equiv\; \mathcal{V}_\infty[M(\boldsymbol{r})]. \tag{4.5}$$

Like with equation (4.2), the velocity field is related to M by a non-local operator, $\mathcal{V}_\infty$. This operator is also linear in M, but it is not anymore scale invariant because the convection system has now an internal length-scale as σ has the dimension of a length,

$$\begin{aligned} \mathcal{V}_\infty[\alpha M] &= \alpha \mathcal{V}_\infty[M] \\ \mathcal{V}_\infty[M(\beta \boldsymbol{r})] &= \beta \mathcal{V}_\infty[M(\boldsymbol{r})]. \end{aligned} \tag{4.6}$$

The reverse transformation that gives the moment as a function of the surface velocity is easy to derive in the real space whatever σ is. The closure law (3.3) can also be written

$$\hat{M}(\boldsymbol{k}) = -2\ \mathrm{i}\frac{1+2\sigma k}{k}\boldsymbol{k}.\hat{\boldsymbol{v}}_H(\boldsymbol{k}), \tag{4.7}$$

which corresponds to

$$M(\boldsymbol{r}) = -4\mathcal{V}_0[\boldsymbol{v}(\boldsymbol{r})] - 4\sigma\boldsymbol{\nabla}\boldsymbol{v}_H, \tag{4.8}$$

(note that the operator $\mathcal{V}_0$ according to its definition (4.2), either maps a scalar to a vector or a vector to a scalar, just like the operator $\boldsymbol{\nabla}$). Equation (4.8) means that the vertical moment of the temperature across the thermal boundary layer can be estimated from the surface velocity on top of the convective medium.

4.2. *Examples of moment-velocity closure relationships*

In 1D, i.e. assuming that $\boldsymbol{v}_H$ and M are only functions of x, the expression (4.2) can be integrated in y, which leads to

$$v_H(x) = \frac{1}{2}\mathcal{H}[M(x)] = \frac{1}{2\pi}\int_{-\infty}^{\infty} \frac{M(x')}{x'-x}\, d\boldsymbol{x}'. \tag{4.9}$$

where the symbol $\mathcal{H}$ stands for the Hilbert transform (Erdélyi 1954). This operator has the same scaling properties (4.3) as its 2D counterpart.

Hilbert transforms of particular functions are tabulated in mathematical handbooks (Erdélyi 1954), see also Table 1 of Thess *et al.* (1997). As a simple example of physical interest, the velocity induced by the field

$$M(x) = \frac{1}{1+x^2}. \tag{4.10}$$

is

$$v_H(x) = -\frac{x}{2(1+x^2)}. \tag{4.11}$$

If the vertical temperature moment is restricted to a singular line, i.e. $M(x) = \delta(x)$, the induced velocity is simply

$$v_H(x) = -\frac{1}{2\pi x}. \tag{4.12}$$

These two solutions are depicted in Figure 4b.

In the case $\sigma \gg 1$, (4.5) integrated in y leads to

$$v_H(x) = \frac{1}{8\sigma}\left(\int_{-\infty}^{x} M(x')\, dx' + \int_{\infty}^{x} M(x')\, dx'\right). \tag{4.13}$$

The velocity induced by the M field (4.10) is

$$v_H(x) = \frac{1}{8\sigma}\arctan(x), \tag{4.14}$$

represented in Fig. 4c. As expected, it is smoother than in the case $\sigma = 0$. The velocity induced by a singular line $M(x) = \delta(x)$ is the step function (written with the Heaviside function H),

$$v_H(x) = \frac{1}{4\sigma}\left(\frac{1}{2} - \mathrm{H}(x)\right). \tag{4.15}$$

We see that when the role of the highly viscous lid becomes important, a uniform velocity is induced on each side of the singular temperature source.

We can also express the closure law in a 2D axisymmetric geometry appropriate to describe plumes. If the vertical temperature moment is restricted to a singular point, $M(\boldsymbol{r}) = \delta(\boldsymbol{r})$ the equations (4.2) and (4.5) become

$$v_r(r) = -\frac{1}{4\pi r^2}, \tag{4.16}$$

when $\sigma = 0$, and with a highly viscous lid at the surface, $\sigma \gg 1$,

$$v_r(r) = -\frac{1}{8\pi\sigma}\frac{1}{r}. \tag{4.17}$$

As in the Cartesian 1D case, the presence of a highly viscous lid increases the effect of a perturbation at large distances.

5. Finite time singularities

Having understood the first stages of the development of an instability we must now study the behavior of the finite time singularities. When a singularity occurs, M goes to $+\infty$ and the last term of equation (3.2), corresponding to the secular diffusive increase of the thermal boundary layer can be safely neglected. In this case we can search for solutions with separate variables of the form

$$M(\boldsymbol{r}, t) = (t_s - t)^a F(\boldsymbol{\chi}), \tag{5.1}$$

where

$$\boldsymbol{\chi} = \frac{(\boldsymbol{r} - \boldsymbol{r}_s)}{(t_s - t)^b}. \tag{5.2}$$

The constants a and b are the critical exponents of the singularity that occurs at position $\boldsymbol{r}_s$ and time t_s.

As the scaling properties of the operator that relates the moment to the horizontal velocity depends on the surface viscosity σ, we first present in details the case $\sigma = 0$ and

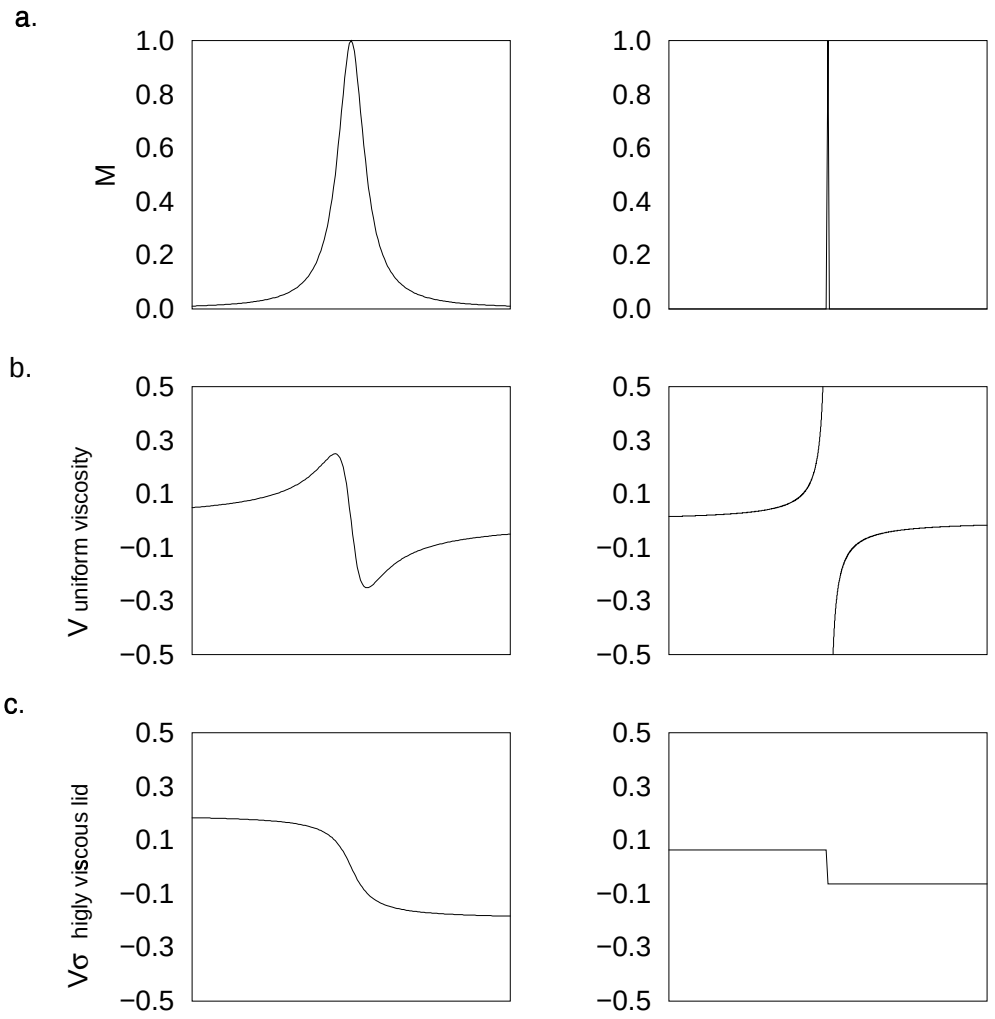

FIGURE 4. *Examples of 1D closure relationships, for* $M(x) = 1/(1+x^2)$ *(left column) and* $M(x) = \delta(x)$ *(right column), M is represented in a., the corresponding velocity with a uniform viscosity* ($\sigma = 0$) *in b., and the velocity with a highly viscous lid* ($\sigma \gg 1$) *in c.*

then discuss the role of the surface viscosity. When $\sigma = 0$, the operator relating moment and velocity is $\mathcal{V}_0$ (4.3) and by plugging (5.1) into (3.2) we get

$$\begin{aligned} &-aF + b\boldsymbol{\chi}\cdot\boldsymbol{\nabla}_H F - (t_s - t)^{-2b+1}\nabla_H^2 F \\ &\quad - (t_s - t)^{a-b+1}(\mathcal{V}_0[F]\cdot\boldsymbol{\nabla}_H F + 2F\boldsymbol{\nabla}_H\cdot\mathcal{V}_0[F]) = 0. \end{aligned} \tag{5.3}$$

Choosing $a = -\frac{1}{2}$ and $b = \frac{1}{2}$, this previous equation becomes time-independent, and

$$M(\boldsymbol{r}, t) = \frac{1}{(t_s - t)^{\frac{1}{2}}} F\left(\frac{\boldsymbol{r} - \boldsymbol{r}_s}{(t_s - t)^{\frac{1}{2}}}\right), \tag{5.4}$$

is solution of equation (3.2) when F verifies

$$F + \boldsymbol{\chi}\cdot\boldsymbol{\nabla}_H F - 2\mathcal{V}_0[F]\cdot\boldsymbol{\nabla}_H F - 4F\boldsymbol{\nabla}_H\cdot\mathcal{V}_0[F] - 2\nabla_H^2 F = 0. \tag{5.5}$$

	uniform viscosity	highly viscous lid
line singularity	$-\frac{A\ln\left(x(t_s-t)^{-\frac{1}{2}}\right)}{2\pi x}$	$-\frac{A\ln\left(x(t_s-t)^{-\frac{1}{2}}\right)}{4\sigma(t_s-t)}$
axisymmetric singularity	$-\frac{B}{2r}$	$-\frac{B}{4\sigma(t_s-t)}$

TABLE 1. Asymptotic velocity at large distance of a singularity

The self-similar solution $M(\boldsymbol{r},t)$ has a maximum diverging as $(t_s-t)^{-\frac{1}{2}}$, and a width decreasing as $(t_s-t)^{\frac{1}{2}}$. For a line singularity (1D geometry), with boundary conditions $\boldsymbol{\nabla}_H F=0$ on the instability and F vanishing at large distance, we find numerically that the solution for F is unique (its shape but also its amplitude). In the 2D axisymmetric case, another solution is obtained as the differential operators entering equation (5.5) are different, but again, this axisymmetric solution, with its shape and its amplitude is univocally obtained by (5.5).

Instead of trying to solve the difficult differential equation (5.5), we have computed numerically in the 1D case $M(x,t)$ for various initial conditions, measured the position x_s and time $t_s$for the first singularity and plotted the quantity $(t-t_s)^{\frac{1}{2}}M(x,t)$ as a function of $(x-x_s)/(t_s-t)^{\frac{1}{2}}$ for times t close to t_s. The results depicted in Figure 5 (top) for four different initial conditions show a universal shape, when properly scaled. Of course, when plotted with a logarithmic scale (bottom), the presence of other weaker growing singularities far from the main one is clearly shown as secondary peaks. We also run 2D axisymmetric cases, similar results are obtained, i.e., the same critical exponents and a unique F solution.

We can use a similar procedure in the case of a highly viscous lid $\sigma \gg 1$, but with the scaling relationship (4.6). This also leads to self-similar solutions of the form

$$M(x,t)=\frac{\sigma}{t_s-t}G\left(\frac{x-x_s}{(t_s-t)^{\frac{1}{2}}}\right). \tag{5.6}$$

where G is another universal function when the geometry, 1D or 2D, is chosen. The maximum now increases as $(t_s-t)^{-1}$, faster than in the case without lid, and its width decreases as $(t_s-t)^{\frac{1}{2}}$.

Figure 6 depicts the same set as in Figure 1 but now, the behavior of $\log(\mathrm{Max}_x M(x,t))$ is plotted as a function of $\log(t-t_s)$. We also show the case with a highly viscous lid ($\sigma \gg 1$). The theoretical laws with exponents -1/2 and -1 are indeed closely followed.

The behavior of M far from a growing instability can be described analytically. In equation (5.5), the terms associated with cross-products between velocity and moment $(-2\mathcal{V}_0[F]\cdot\boldsymbol{\nabla}F-4F\boldsymbol{\nabla}\cdot\mathcal{V}_0[F])$ are smaller than the first two terms if $\mathcal{V}_0[F]\ll\chi$. In this case the solutions of (5.5) are $F(x)\sim A/x$ in the 1D case and $F(r)\sim B/r$ in the axisymmetric case. The proportionality constants A and B are not arbitrary but are univocally determined by the non-linearity of the differential equation close to the singularity. From the shape of the M singularity at large distance, we can use the closure laws (4.2) and (4.5) to deduce the velocity far from the singularity. After some algebra we obtain the asymptotic behaviors summarized in Table 1.

The results of table 1 indicates that singularities interact at very large distance and

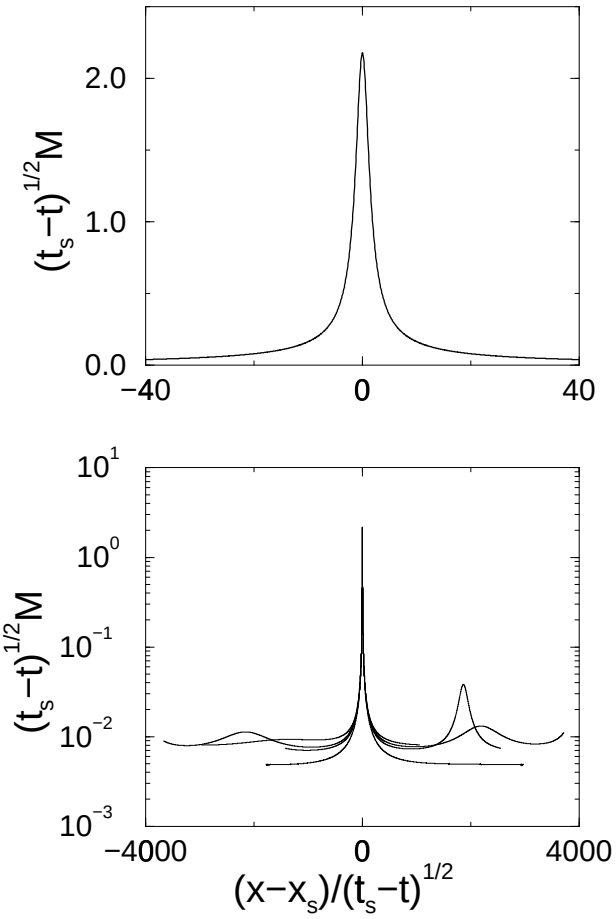

FIGURE 5. *Universal shape of the 1D singularity in the case of a constant viscosity. Four different numerical experiments have been performed and have been rescaled. The bottom curve with a vertical logarithmic scale and a wider spatial extension, shows the presence of other singularities in formation.*

potentially at an infinite distance (highly viscous lid), due to the transport by their induced velocity. Although in figure 4 the velocity induced by a temperature moment decreasing asymptotically as $1/x^2$ remains finite, the natural 1D singularity in a fluid with a highly viscous lid has a temperature moment only decreasing as $1/x$ and therefore induces a velocity diverging as $\ln(x)$. Numerically, the forced periodicity imposed by the use of Fast Fourier Transforms, makes the verification of these laws difficult.

6. Developed convection

6.1. *Regularization of the singularity*

When plumes develop, the temperature heterogeneity θ leaves the boundary layer, so we cannot assume anymore that the θ drops to zero in the range of integration used to get (2.43). Taking into account the value $\theta(Z)$ at the upper bound of integration Z, we

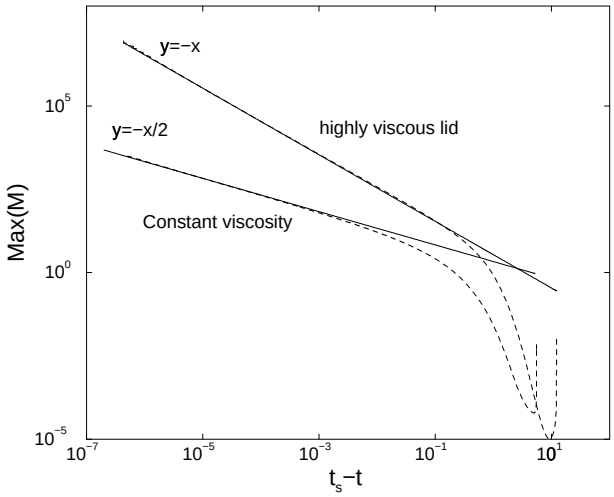

FIGURE 6. *Time behavior of the instability near the singularity in the two cases of constant viscosity or of highly viscous lid. Because the abscissa is $t_s - t$, the singularity now evolves from right to left.*

generalize (2.43) into

$$\frac{\partial M}{\partial t} + (\boldsymbol{v}_H \cdot \boldsymbol{\nabla}_H)M + (2M + Z^2\theta(Z))\boldsymbol{\nabla}_H \cdot \boldsymbol{v}_H = \kappa\nabla_H^2 M - \kappa(\theta_S - \theta(Z)). \qquad (6.1)$$

We need to close this equation to determine $\theta(Z)$ as a function of the dynamical variables. At small times, $\theta(Z) = 0$ and we recover (2.43). In the opposite case of a plume extending beyond the depth Z, the temperature becomes nearly uniform over the depth Z, so we have $Z^2\theta(Z) \simeq Z^2\theta_S \simeq -2M$, so the source terms disappear in (6.1). We propose an heuristic fit between these two extremes, by writing $(2M + Z^2\theta(Z))\boldsymbol{\nabla}_H \cdot \boldsymbol{v}_H = M[1 - \tanh(M - M_{max})]\boldsymbol{\nabla}_H \cdot \boldsymbol{v}_H$, where $M_{max} = -Z^2\theta_S/2$. This provides a regularizing mechanism for the plumes. A corresponding heat injection should be introduced in the interior, providing an additional source of motion. We expect this motion to be at fairly large scales, with a weak influence on the plume dynamics, and we have neglected this modification of the interior in the present study. We also neglect $\theta(Z)$ in the right hand side of the equation (6.1) as this diffusion term is negligible in plumes in comparison with the other effects.

6.2. *Developed convection in the 1D case*

With this regularization mechanism, our model can go beyond the first finite time singularity and a much complex dynamics is obtained. Figure 7 shows the evolution of $M(x)$ at four different times (1D case, with uniform viscosity, $\sigma = 0$). In this simulation we have chosen to cut the singularities around $M_{max} = 30$. The progressive destabilization of the boundary layer starts from the top left panel ($t = 0$) where the arbitrary initial moment has a Gaussian shape. The reader must however realize that the equivalent boundary layer thickness ($(M)^{\frac{1}{2}}$) is of the same order as the horizontal scale.

The first singularities start near the maximum of M (top right) in agreement with the stability analysis. The boundary layer is then destabilized everywhere. For small times (top right and bottom left) the symmetry of the initial conditions is preserved. At larger times, (bottom right), the symmetry is broken by the birth of new instabilities.

In order to more clearly understand the initiation and interactions of instabilities,

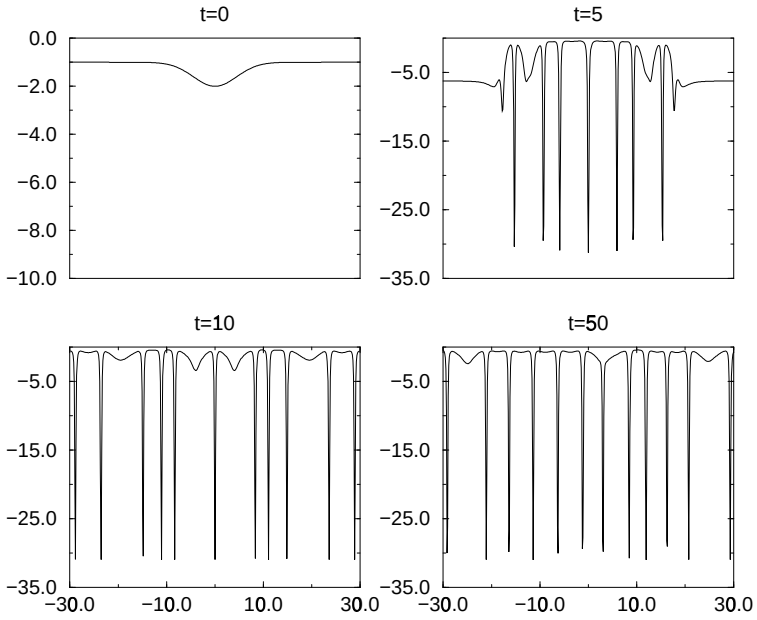

FIGURE 7. *Growth and dynamics of 1D instabilities, $M(x,t)$ as a function of x at four different times t.*

Figure 8 depicts the position of the peaks as a function of time for the same simulation as in Figure 7. At the beginning, a large number of peaks is produced, this number then reduces to about 10 peaks. This reduction follows the reduction of the average boundary layer thickness. This corresponds qualitatively to the fact that the wavelength of the most unstable perturbation in the marginal stability study increases when the average thickness decreases.

The various peaks attract each others. When two peaks merge, a new peak appears in the space left empty. Because of this chaotic behavior, the pattern loses its symmetry after a time larger than 30 in this simulation. The number of peaks is then rather constant in average and close to one peak every 2π (i.e. about 10 peaks in this simulation where the abscissae goes from -10π to 10π) .

The characteristic parabolic shape of the trajectories of two peaks in interaction is easy to understand at least qualitatively following a method originally applied to Marangoni convection (Thess *et al.* 1995, 1997). Each peak induces in its vicinity an attractive velocity $v_H(x)$, transporting its neighborhood, so that the distance X between them varies as

$$\frac{dX}{dt} = 2v_H(X). \tag{6.2}$$

If we assume that the two peaks are close enough to interact but far enough so that each one induces a velocity as if it were alone (vortex dynamics, Aref 1983), then the attractive velocity can be computed. At 1D and $\sigma = 0$, the closure law needs the introduction of the Hilbert transform of the moment of the instability (4.9). This closure law can be written in a different form, that has the advantage of using defined integrals rather than

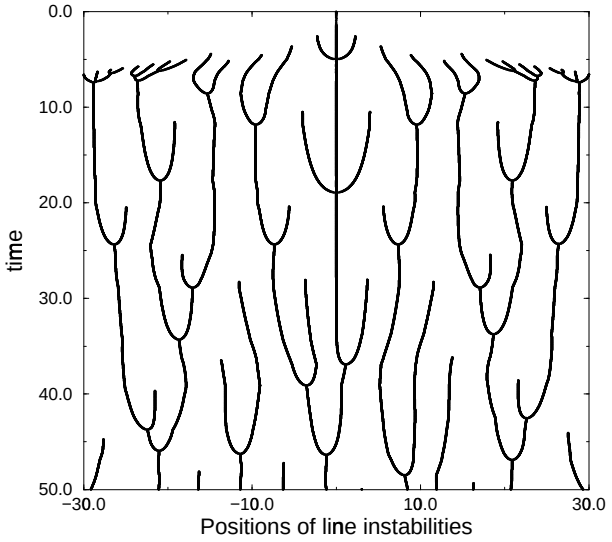

FIGURE 8. *Positions of the line instabilities of Figure 7 as functions of time.*

Cauchy improper integrals,

$$v_H(X) = \frac{1}{2\pi} \int_0^\infty \frac{M(X+x') - M(X-x')}{x'}\, dx'. \tag{6.3}$$

The numerator varies much more rapidly around $x' = X$ than the denominator and far from this point the numerator is very small. Therefore, we can approximate the $1/x'$ under the integral sign, by $1/X$ and, using the parity of $M(x)$, we get

$$v(X) \sim \frac{1}{2\pi X} \int_0^\infty M(X+x') - M(X-x')\, dx' = -\frac{1}{2\pi X} \int_{-X}^{X} M(x)\, dx. \tag{6.4}$$

When the heads of the instabilities are cut beyond a limited range, this last integral is roughly a constant I_0 and thus

$$\frac{dX}{dT} = -\frac{I_0}{\pi X}, \tag{6.5}$$

or,

$$X^2 = X_0^2 - 2\frac{I_0}{\pi} t \tag{6.6}$$

where X_0 is the initial distance between peaks. This last equations explains the parabolic trajectories occurring when two peaks collapse. When the instabilities are not limited by a maximum size M_{max}, the distance between two isolated peaks can still be closely fitted on a limited range of distances by a parabolic law although we know that the integral in the equation (6.4) slowly diverges as $\ln(X/(t_s - t)^{\frac{1}{2}})$ in agreement with Table 1.

We closely verified the previous equations (6.4-6.6) in the presence of two isolated peaks. However, this situation is not stable and soon other peaks appear. Quantitatively, we can extract from Figure 8, a value I_0 that gives the best fit to the behavior of the trajectories when they merge. We found a value of about 4 times smaller than the integral of each singularity. This discrepancy has not been understood although we think that it is not produced by the approximation of (6.4) but rather by a collective effect due to the

other instabilities interacting at large range. It is remarkable that a same parameter I_0 seems to characterize all the interactions of two peaks.

6.3. *Developed convection in the 2D case*

In two dimensions, we also run our program starting from initial conditions

$$M(x,y,0) = 4 + \cos(4\pi y/L)\cos(2\pi x/L) + \sin(2\pi x/L)\sin(2\pi y/L) + \cos(4\pi y/L)\sin(6\pi x/L) \tag{6.7}$$

where the size of the box L is 5. This functional dependence (except for the mean value equal to 4) was used by Thess *et al.* (1997) in their study of Marangoni convection. We verified that our program exactly reproduces their results when the term that contains $\boldsymbol{\nabla}_H \cdot \boldsymbol{v}_H$ is suppressed in equation (6.1), and when the thermal diffusivity is small. In the case of Rayleigh-Bénard convection with only cooling from above, figure 9 depicts various results as a function of time. We only show the case $\sigma = 0$ in this simulation. As seen on the closure relationship (2.41), increasing σ tends to smooth the velocity field and eases the computation. As in 1D geometry, we first observe the increase of the boundary layer thickness and the growth of instabilities that keep the geometry of the initial conditions (top row). The cold plumes and sheets start attracting each other according to the mechanism already discussed (middle row). The initial conditions are still reminded in the pattern of convection. The merging of some instabilities liberates enough space for a new instability to occur as a plume structure in the middle of a roughly hexagonal cell (bottom left). At a later stage, the memory of the initial geometry is totally lost (bottom right) but the topological characteristics of the convection pattern (i.e. the number of cells, the length of cold downwellings...) remain the same.

6.4. *Nusselt-Rayleigh relationship*

In a usual convection experiment, i.e., a liquid tank of height L, where a temperature difference ΔT is imposed between the surface and the bottom, the convective activity can be estimated by two non-dimensional numbers. The first is the Rayleigh number Ra, the normalized temperature difference, and the second is the Nusselt number Nu, the heat flux Q normalized by the heat flux that would occur by pure conduction. These two numbers are

$$\mathrm{Ra} = \frac{\alpha \rho_0 g \Delta T L^3}{\eta_0 \kappa}, \tag{6.8}$$

and

$$\mathrm{Nu} = \frac{LQ}{\kappa \rho_0 C_p \Delta T}, \tag{6.9}$$

(the thermal conductivity is $\kappa \rho_0 C_p$ where C_p is the heat capacity). These two numbers are related by the dynamics, and we expect a model of convection to yield this relationship.

In our model, the flow is entirely driven by boundary layer effects, with no influence of the thickness L, which is supposed very large. Then the only possible relationship, which does not depend on L, is

$$\mathrm{Nu} = a\ \mathrm{Ra}^{\frac{1}{3}}, \text{with } a = \frac{Q}{\kappa \rho_0 C_p \Delta T}\left(\frac{\eta_0 \kappa}{\alpha \rho_0 g \Delta T}\right)^{\frac{1}{3}} \tag{6.10}$$

In our model, Nu and $Ra^{\frac{1}{3}}$ are both infinite, being both proportional to the thickness L, but the constant a is well defined and can be calculated as follows.

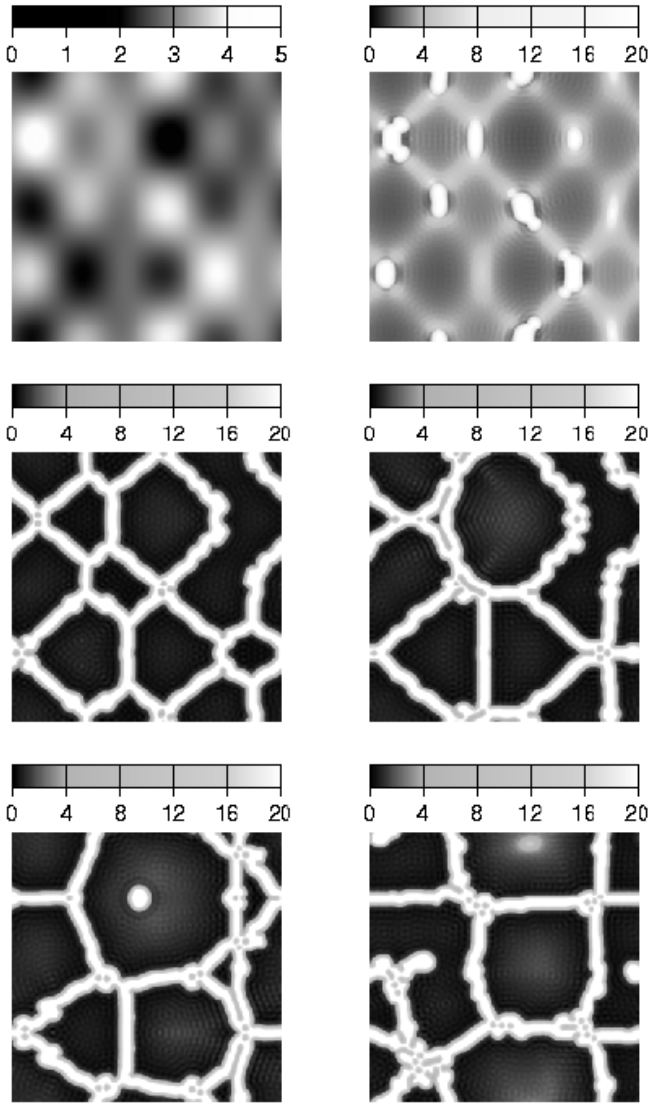

FIGURE 9. *Rayleigh-Bénard convection with uniform viscosity for a fluid cooled from above. top left is the initial condition, top right is at t=1, middle left, t=4, middle right, t=8, bottom left, t=13.5 and bottom right, t=30.*

The average surface heat flow is given by

$$Q = -\kappa\rho_0 C_p \frac{1}{S}\int_S \frac{\partial\theta}{\partial z}\, dS, \tag{6.11}$$

where the integration is performed at the surface S of the convective fluid. Our model

deals with the variable M, the first moment of the temperature in the boundary layer, and we need to make some hypothesis on the vertical temperature profile to calculate the heat flux (6.11). At short times, temperature satisfies the diffusion equation, and varies with z like a complementary error function, therefore $\theta = \theta_s \mathrm{erfc}(z/H)$ where H is the thickness of the boundary layer and $\partial_z \theta = -2\theta_s/(\pi^{\frac{1}{2}} H)$. Using (2.44) that relates M and H ($M = -\theta_s H^2/4$), we get then

$$Q = \kappa \rho_0 C_p \frac{1}{S} \int_S \frac{(-\theta_S)^{\frac{3}{2}}}{(\pi M)^{\frac{1}{2}}}\, dS. \tag{6.12}$$

This last dimensionalized expression can be written with an adimensionalized M as

$$Q = -\kappa \rho_0 C_p \theta_S \left(\frac{-\alpha \rho_0 g \theta_S}{\eta_0 \kappa}\right)^{\frac{1}{3}} \frac{1}{S} \int_S \frac{1}{(\pi M)^{\frac{1}{2}}}\, dS, \tag{6.13}$$

or by the introduction of a dummy length L, and noting that $\Delta T = -2\theta_S$ since we need to symmetrize the system with 2 boundary layers to fit with the usual Rayleigh-Bénard configuration,

$$\mathrm{Nu} = \left(\frac{1}{S} \int_S \frac{1}{2^{\frac{4}{3}} (\pi M)^{\frac{1}{2}}}\, dS\right) \mathrm{Ra}^{\frac{1}{3}}, \tag{6.14}$$

in agreement with the functional form of equation (6.10).

Figure 10 depicts the average over the surface of $(2)^{-\frac{4}{3}} (\pi M)^{-\frac{1}{2}}$, as a function of time, in the 1D case (solid line), and 2D case (dashed line), these two simulations have been performed with $M_{max} = 30$. In the 1D case, the initial conditions are simply a very small M, in the 2D case, we use the same boundary conditions as in figure 9. In the 1D case, at the beginning, the thermal boundary thickness is very small and grows by simple diffusion following a $t^{-\frac{1}{2}}$ law (thin solid line). This behavior is not as clearly seen for the 2D case, as we already start in a regime where the boundary layer is unstable. When the convection starts the heat flow increases and then stabilizes around $\mathrm{Nu}/\mathrm{Ra}^{\frac{1}{3}}$ close to .22.

The mean value of $Nu/Ra^{\frac{1}{3}}$ is slightly dependent of the choice of M_{max} (figure 11), it increases from 0.165 for $M_{max} = 10$ to 0.235 for $M_{max} = 40$ (1D case), the numerical experiment may indicate an asymptotic value for very large M_{max}. However there may be no truly asymptotic value, which would reflect some departure to the $Ra^{\frac{1}{3}}$ law. Indeed we may expect that the thickness $\sim M^{\frac{1}{2}}$ associated with the maximum possible value of M scales with the thickness L.

Our Rayleigh-Nusselt relationship can be compared with results found in the literature. For convection at infinite Prandtl number, and heated from below, simple boundary layer models (Turcotte & Oxburg, 1967) give $Nu \sim 0.294\ Ra^{\frac{1}{3}}$.2D and 3D numerical simulations (McKenzie, Roberts & Weiss, 1974; Travis, Olson & Schubert, 1990; Tackley, 1996; Sotin & Labrosse, 1999) and laboratory experiments at very high Prandtl number (Giannandrea & Christensen, 1993; Manga & Weeraratne, 1999) provide similar values (although the exponent seems smaller than 1/3). Laboratory experiments by Goldstein, Chiang & See (1990) give $Nu \sim 0.066\ Ra^{\frac{1}{3}}$ but for no slip boundary conditions and a moderate Prandtl number.

7. Conclusion

We have shown that the equations of 3D convection in the limit of high Rayleigh and Prandtl numbers can be reduce to 2D equations written at the surface of the convective fluid. These equations express how the moment of the temperature through the thermal

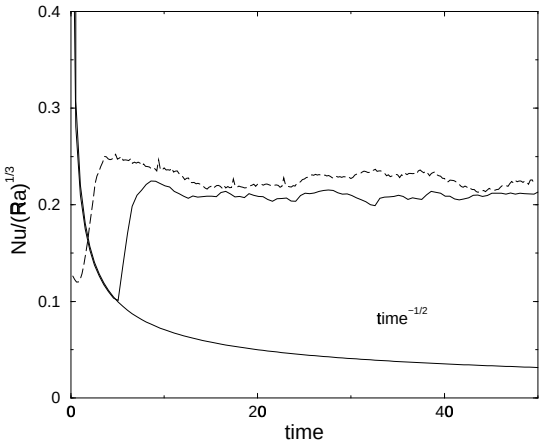

FIGURE 10. *Evolution of Nusselt/Rayleigh$^{\frac{1}{3}}$ as a function of time, in 1D (solid line) and 2D (dashed line) simulations.*

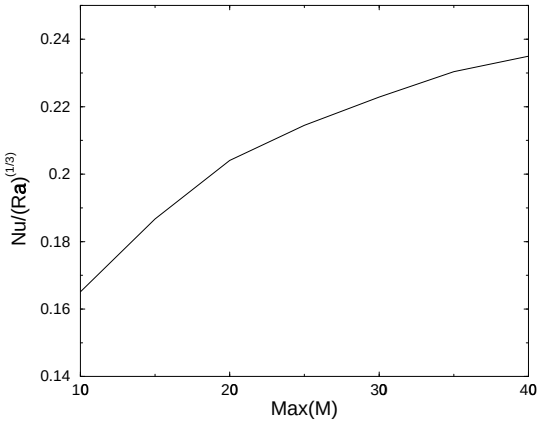

FIGURE 11. *Dependence of the Nusselt number with the maximum moment M_{max}.*

boundary layer is transported and modified by the surface 2D velocity field. They are universal, i.e. they do not contain any physical parameters. This reduction from 3D to 2D provides an elegant tool to study the initiation of thermal plumes and line instabilities.

Various generalizations of the present theory can be done in a straightforward manner. The role of a depth-dependent viscosity in the thermal boundary layer is controlled by a parameter σ. However we could have also considered depth-dependent viscosity variations in the deep interior. As an example the viscosity of silicated planets increases significantly with depth. This can be very easily taken into account by a modification of the closure law. Another modification of the closure law could allow us to study the interaction of a top boundary layer with a bottom boundary layer. In this case two transport equations would have be coupled through two closure laws relating linearly in the spectral space the surface velocity of each boundary layer to the two temperature moments.

Apart from its utility to understand the development of instabilities, their interactions, the similarities and differences between Marangoni convection and thermal convection,

our approach suggests a method to study a very important geophysical problem, namely the interactions between plate tectonics and the underlying high Rayleigh number convection. In our planet, the rheology of the surface boundary layer is highly non-linear and therefore the present theory does not apply. However, we have purposely used as long as possible, stresses rather than velocities in deriving the equations of this paper in order to distinguish what is related to the assumption of a Newtonian rheology and what is perfectly general. The relationships between stresses and temperature moment (2.20, 2.21) and the transport equation (2.43) are independent of the rheology. This means we are able to reduce the 3D hydrodynamic problem of plate tectonics to 2D surface equations even in the case of a very complex relationship between stresses and velocities. Of course, in this case the equivalent of the closure relationship will be only obtained numerically and a vertical vorticity would potentially be excited.

We would like to thank Frédéric Chambat for his friendly help in the development of this work. This work has benefited from useful discussions with A. Thess in the frame of the french-german collaboration program DFG/CNRS under Grant th497/11-1. It has been supported by the CNRS-INSU programs. The computation have been performed on the PSMN computing facilities.

REFERENCES

AREF, H. 1983 Integrable, chaotic, and turbulent vortex motion in two-dimensional flows. *Ann. Rev. Fluid. Mech.* **15**, 345–389.

BATCHELOR, G.K. 1954 Heat convection and buoyancy effects in fluids. *Quart. J. R. Met. Soc.* **80**, 339–358.

BIRD, P. 1954 Formation of the Rocky Mountains, Western United States: A Continuum Computer Model *Science* **238**, 1501–1507.

CANRIGHT, D. & MORRIS, S. 1993 *J. Fluid. Mech.* **255**, 349–372.

CHANDRASEKHAR, S. 1981 *Hydrodynamic and hydromagnetic stability.* Dover.

BERCOVICI, D. AND RICARD, Y. AND RICHARDS, M. 1998 The relation between mantle dynamics and plate tectonics : A somewhat biased primer. *J. Geophys. Res.* (submitted)

ENGLAND, P.C. & MCKENZIE, D.P. 1982 A thin viscous model sheet model for continental deformation. *Geophys. J. R. Astron. Soc.* **70**, 295–322.

ERDÉLYI, A. 1954 *Tables of Integral Transforms.* McGraw Hill.

FLEITOUT, L. & FROIDEVAUX, C. 1982 Tectonic and topography for a lithosphere containing density heterogeneities. *Tectonics* **1**, 21–56.

FLEITOUT, L. & FROIDEVAUX, C. 1983 Tectonic stresses in the lithosphere. *Tectonics* **2**, 315–324.

GIANNANDREA, E. & CHRISTENSEN, U. 1993 Variable viscosity convection experiments with a stress-free upper boundary and implications for the heat transport in the earth's mantle. *Phys. Earth Planet Inter.* **78**, 139–152.

GOLDSTEIN, R.J., CHIANG, H.D. & SEE,D.L. 1990 High-Rayleigh-number convection in a horizontal enclosure. *J. Fluid. Mech.* **213**, 111–126.

HOUSEMAN, G. & ENGLAND, P. 1986 A dynamical model of lithosphere extension and sedimentary basin formation. *J. Geophys. Res.* **91**, 719–729.

HOWARD, L.N. 1966 Convection at high Rayleigh number. In *Proc. II. Int. Congree Appl. Mech.* (ed. H. Goertler). pp. 1109–1115. Springer.

MCKENZIE, D.P., ROBERTS, J.M. & WEISS, N.O. 1974 Convection in the earth's mantle: towards a numerical simulation *J. Fluid. Mech.* **62**, 465–538.

MANGA, M. & WEERARATNE, D. 1999 Experimental study of non-Boussinesq Rayleigh-Bénard convection at high Rayleigh and Prandtl numbers. *Phys. Fluids* **11**, 2969–2976.

MOSES, E., ZOCCHI, G. & LIBCHABER, A. 1993 An experimental study of laminar plumes. *J. Fluid. Mech.* **251**, 581–601.

NATAF, H.C. 1991 Mantle convection, plates, and hotspots. *Tectonophysics* **187**, 361–371.

Olson, P., Schubert, G. & Anderson, C. 1993 Structure of axisymmetric plumes. *J. Geophys. Res.* **98**, 6829–6844.

Pozrikidis, C. 1992 *Boundary Integral and Singularity Methods for Linearized Viscous Flow.* Cambridge.

Ricard, Y., Fleitout, L. & Froidevaux, C. 1984 Geoid heights and lithospheric stresses for a dynamic Earth. *Annales Geophysicae* **2**, 267–286.

Siggia, E.D. 1994 High Rayleigh number convection. *Ann. Rev. Fluid Mech.* **26**, 137–168.

Sotin, C. & Labrosse, S. 1999 Three-dimensional thermal convection in an iso-viscous, infinite Prandtl number fluid heated from within and from below : applications to the transfer of heat through planetary mantles. *Phys. Earth Planet. Int.* **112**, 171–190.

Sparrow E.M., Husar, R.B. & Goldstein, R.J. 1970 Observations and other characteristics of thermals *J. Fluid Mech.* **41**, 793–800.

Tacley, P.J. 1996 Effects of strongly variable viscosity on three-dimensional compressible convection in planetary mantles *J. Geophys. Res.* **101**, 3311–3332.

Thess, A., Spirn, D. & Jüttner, B. 1995 Viscous flow at infinite Marangoni Number. *Phys. Rev. Lett.* **75**, 4614–4617.

Thess, A., Spirn, D. & Jüttner, B. 1997 A two-dimensional model for slow convection at infinite Marangoni number. *J. Fluid. Mech.* **331**, 283–312.

Travis, B., Olson, P. & Schubert, G. 1990 The transition from two-dimensional to three-dimensional planforms in infinite-Prandtl-number thermal convection. *J. Fluid. Mech.* **216**, 71–91.

Turcotte, D.L. & Oxburgh, E.R. 1967 Finite amplitude convection cells and continental drift. *J. Fluid. Mech.* **28**, 29–42.

Vilotte, J.P. & Daignières, M. 1982 Numerical modeling of intraplate deformation: simple mechanical models of continental collision. *J. Geophys. Res.* **87**, 10,709–10,728.